Active Vibration Control of a Flexible Rotor by Flexibly-Mounted Internal-Stator Magnetic Actuators

Chris Lusty and Patrick Keogh

***Abstract*—This paper demonstrates vibration reduction in a hollow rotating shaft by means of internal-stator active magnetic actuators, which are resiliently mounted. This problem requires further consideration over and above classic rotor / magnetic bearing systems on account of the flexible behavior of the magnetic actuator support structure. The paper presents an experimental facility conforming to the proposed topology, with a particular focus on the control problem such a system presents. The unique challenges are discussed, and a solution is presented in the form of H_∞ based control. Ultimately, experimental results demonstrate the system to be capable of substantial rotor vibration suppression, including while passing the first rotor critical speed, which was not obtainable with simpler classical control techniques. This means the top achievable rotor speed was increased from approximately 3000 rpm without magnetic actuator vibration suppression to over 9000 rpm with vibration suppression active. At the rotor critical speed, the magnetic actuators effect a reduction in rotor vibration amplitude of over 70% compared to the rotor supported purely on mechanical bearings, while simultaneously avoiding excessive excitation of the flexible AMB support structure.**

I. Introduction

THE challenge of analyzing, controlling and minimizing vibration in rotating shafts has been given substantial consideration in the literature since the early works of Rankine [1], Föppl [2], Dunkerley [3] and Jeffcott [4]. Advances in various electrical and computational capabilities underpinned by developments in semiconductor technology have permitted the emergence of Active Magnetic Bearings (AMBs). Early works in the magnetic bearing field, such as those of Habermann and Liard [5], Schweitzer [6] and Burrows et al. [7] focused on the problem of achieving stable levitation of rotating shafts, initially for rigid rotors and subsequently extending to rotors exhibiting flexible behavior. Other early work considered the closely related task of using a magnetic actuator as a supplementary bearing on a rotor which is already fully supported by passive bearings. The magnetic actuator in these applications was dedicated to the task of vibration reduction. This can be seen in the work of Nikolajsen et al. [8] for a flexible transmission shaft and Kasarda et al. [9] for a similar shaft carrying multiple heavy disks. In addition to vibration reduction and an ability to support very high speed rotors, magnetic bearings are well known to offer a range of other advantages over traditional bearings, including no lubrication requirements, no friction losses or wear and long, low maintenance service life.

C. Lusty and P. Keogh are with the Department of Mechanical Engineering, University of Bath, UK, e-mail: C.Lusty@bath.ac.uk

This work was supported by the James Dyson Foundation.
Manuscript submitted for review Oct, 2017

Many authors have focused attention on subaspects of the magnetic bearing field, from combining magnetic bearings with other types in a single hybrid device [10, 11], the use of magnetic bearings in specific technology areas [12, 13, 14], operating techniques to improve energy efficiency [15, 16], and the use of magnetic bearings as a combination of both sensor and actuator [17, 18, 19].

A review of important work in the progress of machinery employing active bearings is provided by Burrows et al. [20], while practical advice for designing and using magnetic bearings is provided by Maslen et al. [21].

It is notable that across the published work on magnetic bearing systems, a standard overall topology is commonly used, whereby the magnetic actuators are located external to the rotor, and are rigidly mounted to the machine base. This permits the magnetic actuators to be designed with little constraint on their overall physical size, but has the disadvantage of utilizing a substantial axial length of the rotor, which might otherwise be used for other machine working elements. This issue is highlighted by Stanway and Burrows [22], who consider the control of rotor vibration in the case that there are practical placement constraints on the location of an actuator (e.g. magnetic bearing), as is the case in real industrial machinery. Further options have been considered in [23] using μ-synthesis for controller design, and [24], for design optimization with the inclusion of eddy current effects in high-speed systems.

A limited number of authors have considered concepts whereby the magnetic bearing stator is located inside of a hollow rotor, for example in energy storage flywheels and bearingless and high-speed motors [25, 26, 27, 28, 29]. However, it is still generally considered that the AMB stator is rigidly located to the machine base. With these applications, the rotor operates sub-critically.

It is proposed that one pathway to novel machine designs which permits the inclusion of AMBs, with their attendant performance advantages, into compact high speed rotor systems while circumventing the space penalty of traditional AMB designs is to employ internal-stator AMBs inside hollow-shaft rotors. A consequence of such a layout is that the AMB will be supported on a long, thin structure which will exhibit its own flexible behavior (in addition to any flexibility of the rotor). While in some cases material yield strength may limit the top speed of large diameter hollow rotors, in many other cases the top speed is limited by other factors such as vibration and bearing performance. This work aims to facilitate improved performance in such designs. Similarly, diametral enlargement of hollow shaft rotors due to centrifugal force, and the consequential widening of the air gap for an internal

stator AMB is a potential disadvantage not faced by more common external stator AMB machines. However, the effect is not severe enough to prevent successful applications of high-speed, hollow shaft rotors, for instance as recently discussed by Quurck et al. [30].

The authors have presented [31] initial conceptual modeling of an arbitrary system based on this concept, demonstrating the potential capacity of the flexibly-mounted, internal-stator magnetic actuator to influence a rotor system's dynamic characteristics. In [32], they present an experimental facility to explore the practical implementation of such a scheme. Some limited initial testing on the experimental facility using classical control techniques is presented, however only minor performance improvements are achieved via the AMBs when compared to the basic uncontrolled rotor. A key factor underpinning the lack of significant performance gains under traditional control is that both the rotor and the magnetic actuator support structure exhibit flexible behavior. Thus the displacement transducers mounted adjacent to the magnetic actuators report a *relative* displacement between these two bodies, which is used as the error signal which the controller attempts to minimize. However, the performance goal is for the AMBs to minimize the *absolute* displacement of the rotor, while ensuring that contact between the rotor and the AMBs is avoided.

This paper demonstrates how the performance potential of flexibly-mounted, internal-stator AMB systems may be unlocked through the use of a model-based control strategy. The design is based on an H_∞ controller which is capable of reducing the absolute vibration of the rotor when provided only with relative motion displacement signals. A set of experimental test results give a clear demonstration of the system performance enhancements achieved through the use of the H_∞ controller, including safe transition through rotor's first critical speed, which was not possible with either the uncontrolled or the classically controlled system.

II. Experimental Facility

A three part steel rotor with variable cross-section is used, as illustrated in Figure 1. The rotor has a pair of large-diameter hollow sections at either end, connected by a thin solid section in the middle. The thin section ensures the rotor's first critical speed is sufficiently low to be sensibly achieved in laboratory testing. The hollow tube sections at each end accommodate the magnetic bearings. The techniques developed in this work are not specific to this topology, however, which is used here purely for its convenience for laboratory investigation. The techniques are applicable to any hollow flexible rotor, whether the flexibility stems from narrow cross section elements, long rotor length, presence of large disc elements etc.

As seen in Figure 1, the rotor is supported on rolling element bearings at its ends; in principle these could be removed and the rotor fully levitated on the internal magnetic bearings, although in the present case the rolling element bearings are left in place and the focus is on the use of the magnetic actuators for vibration control. As such, all displacement of the rotor in this work results from the rotor's flexible characteristics,

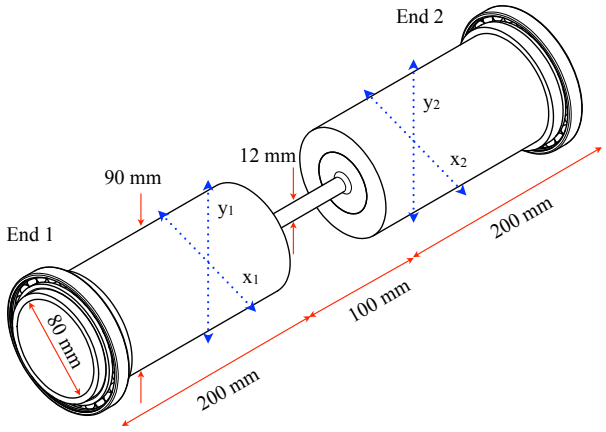

Fig. 1. Outline view of variable diameter steel rotor showing major dimensions and axes of acutation

TABLE I
Key parameters of magnetic actuators

Parameter	Value	Parameter	Value
Maximum force	43 N	Coil inductance	2.7 mH
Bias current	2 A	Current gain	13.7 N/A
Peak current	4 A	Displacement gain	38 kN/m
DC link voltage	120 V		

with rigid body motion constrained by the rolling element bearings, as seen in various other studies [8, 9, 33]. The system includes two similar magnetic actuator subassemblies, which are inserted into the hollow end sections of the rotor. These subassemblies are located at the ends of cantilevered beams, termed secondary shafts, which are anchored independently to a base plate. The cantilever beams behave flexibly since they exhibit natural frequencies within the operating rotational speed range of the system; they are therefore liable to be excited in resonance. Each subassembly at the end of the cantilevers includes a pair of orthogonally mounted eddy current displacement transducers adjacent to the magnetic actuator for use in the control feedback loop. On the other side of each magnetic actuator is a brass disk, which functions as a touchdown surface in the case of unintended rotor/stator contact. These components, located on the shaft between a pair of clamping collars, are illustrated in Figure 2. A diagram showing a magnetic actuator subassembly inserted into the rotor as per operation is provided in Figure 3. A photograph clarifying the assembly process and operational positioning of the magnetic actuator subassemblies is provided in Figure 4.

The magnetic actuators are of homopolar design, in order that induced eddy currents in the rotor can be kept to a minimum without having to use a laminated collar within the rotor. This maximizes the space available for the magnetic actuators, thus maximizing the obtainable force capacity. The actuator stators are fabricated from Soft Magnetic Composite (SMC), which minimizes stator-based eddy currents and heat generation inside the rotor, while also allowing the stator to be manufactured as a single piece, permitting a highly space efficient geometry. Key magnetic actuator parameters are shown in Table I.

Several further details of the experimental facility design

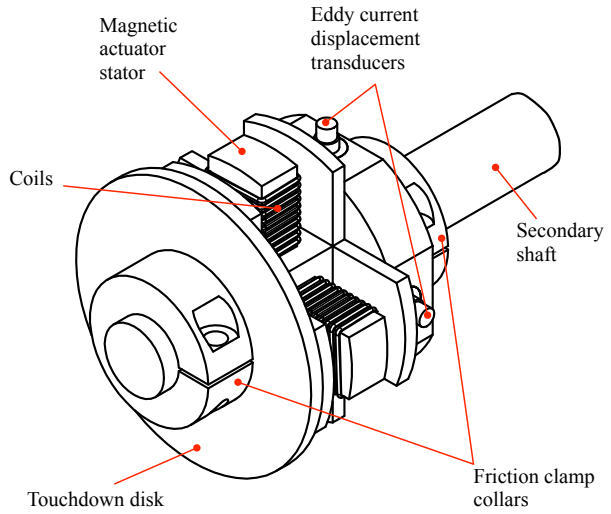

Fig. 2. Internal-stator magnetic actuator and associated parts mounted on the secondary shaft

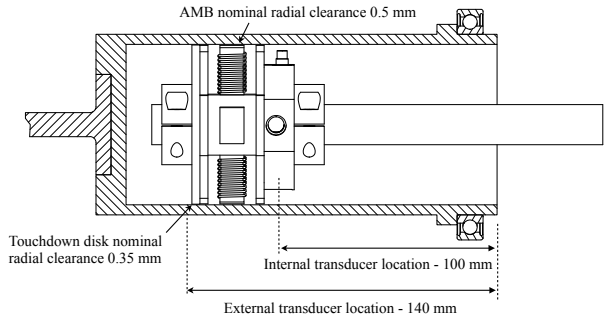

Fig. 3. View showing half the rotor with a magnetic actuator in operational position

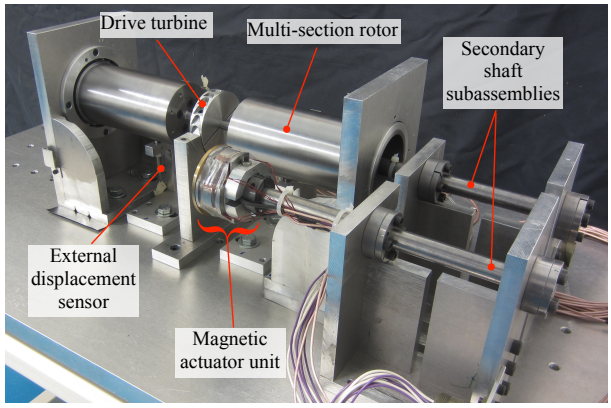

Fig. 4. Photograph showing partially assembled experimental facility. The rotor is seen in the background with one secondary shaft inserted in the operational position. The other secondary shaft is seen in the foreground, aligned to help visualize the operational arrangement.

can be observed in Figure 4. The rotor is driven by an impulse turbine fed from a compressed air supply at its midspan. The system also includes four external eddy current transducers. These are mounted rigidly to the rig base, and measure the absolute displacement of the rotor in orthogonal axes at two locations along the rotor span. These are not used for feedback, but only to monitor rotor displacements. These external transducers do not lie in the same planes as the internal transducer pairs; due to spatial considerations the externally mounted sensors are located further towards the rotor center section, as indicated in Figure 3.

III. System Model

A model was initially generated via standard finite element techniques, as presented by Nelson and McVaugh [34]. Accordingly, an equation of motion incorporating all three of the members of this system (rotor and two secondary shafts) may be presented as

$$\mathbf{M}\ddot{\mathbf{q}} - \Omega\mathbf{G}\dot{\mathbf{q}} + \mathbf{K}\mathbf{q} = \mathbf{f} \tag{1}$$

where

$$\mathbf{M} = \underbrace{\begin{bmatrix} \mathbf{M}_R & \mathbf{0} & \mathbf{0} \\ \mathbf{0} & \mathbf{M}_{S1} & \mathbf{0} \\ \mathbf{0} & \mathbf{0} & \mathbf{M}_{S2} \end{bmatrix}}_{100\times100}, \quad \mathbf{G} = \underbrace{\begin{bmatrix} \mathbf{G}_R & \mathbf{0} & \mathbf{0} \\ \mathbf{0} & \mathbf{0} & \mathbf{0} \\ \mathbf{0} & \mathbf{0} & \mathbf{0} \end{bmatrix}}_{100\times100}$$

$$\mathbf{K} = \underbrace{\begin{bmatrix} \mathbf{K}_R & \mathbf{0} & \mathbf{0} \\ \mathbf{0} & \mathbf{K}_{S1} & \mathbf{0} \\ \mathbf{0} & \mathbf{0} & \mathbf{K}_{S2} \end{bmatrix}}_{100\times100}, \mathbf{q} = \begin{bmatrix} \mathbf{q}_R \\ \mathbf{q}_{S1} \\ \mathbf{q}_{S2} \end{bmatrix}, \mathbf{f} = \begin{bmatrix} \mathbf{f}_R \\ \mathbf{f}_{S1} \\ \mathbf{f}_{S2} \end{bmatrix}$$

In line with common notation, $\mathbf{M}$, $\mathbf{G}$ and $\mathbf{K}$ are respectively mass, gyroscopic and stiffness matrices, and $\mathbf{q}$ and $\mathbf{f}$ are vectors of degrees of freedom and applied forcing. The subscripts $_R$, $_{S1}$ and $_{S2}$ denote the rotor and each of the secondary shafts respectively, and Ω is the rotor spin speed.

In this case, the rotor is modelled by 12 elements such that $[\mathbf{M}, \mathbf{G}, \mathbf{K}]_R$ are each size 52×52, and the secondary shafts are modelled by 5 elements each, such that $[\mathbf{M}, \mathbf{G}, \mathbf{K}]_{Sx}$ are each size 24×24.

In addition to the standard rotor finite element units, terms are included in the stiffness matrix to represent the clamping of the secondary shaft and the rolling element bearings of the rotor. Terms are also included in the mass and, where appropriate, gyroscopic matrices to represent the magnetic actuator subassemblies on the secondary shafts, the drive turbine on the rotor and also the additional material where the individual rotor sections are connected together.

Damping effects are modelled by the addition of equivalent viscous dampers. These are added at the tip of each secondary shaft and at the center of the rotor to account for the effects of both internal damping and support structure damping.

For modeling and simulation tasks, Equation (1) is arranged into state space form as

$$\begin{aligned} \dot{\mathbf{z}} &= \mathbf{A}\mathbf{z} + \mathbf{B}\mathbf{f} \\ \mathbf{y} &= \mathbf{C}\mathbf{z} \end{aligned} \tag{2}$$

where

$$\mathbf{z} = \begin{bmatrix} \mathbf{q} \\ \dot{\mathbf{q}} \end{bmatrix}, \quad \mathbf{A} = \begin{bmatrix} \mathbf{0} & \mathbf{I} \\ -\mathbf{M}^{-1}\mathbf{K} & \Omega\mathbf{M}^{-1}\mathbf{G} \end{bmatrix}, \quad \mathbf{B} = \begin{bmatrix} \mathbf{0} \\ \mathbf{M}^{-1} \end{bmatrix} \hat{\mathbf{B}}$$

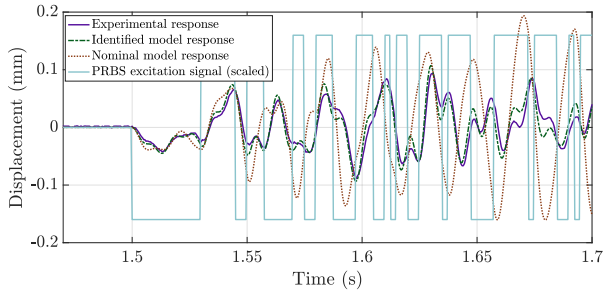

(a)

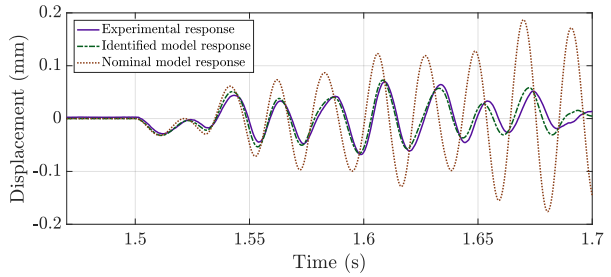

(b)

Fig. 5. Simulated response of plant model to PRBS excitation compared with experimental rig response to same excitation; a) as seen by internal sensor in x_1 axis, b) as seen by external sensor in x_1 axis (see Figure 1)

and $\mathbf{y}$ is a subset of $\mathbf{z}$ selected by the binary matrix $\mathbf{C}$. $\hat{\mathbf{B}}$ is a binary matrix, and together with $\mathbf{C}$ is used to tune the model such that control inputs are only applied at locations where the magnetic bearings act, and feedback signals are only taken at locations where sensors are placed.

A parameter optimization was undertaken on the model in order to match its behavior to the experimentally observed behavior of the physical system. The technique used was based on work presented by Lauridsen et al. [35], involving the minimization of a cost function which expresses the difference between the simulated and experimental responses of the system to a given excitation. Figure 5 demonstrates the results of this process, comparing the simulated model response to a pseudo random binary sequence (PRBS) excitation before and after the identification process with the response of the experimental rig. A significant improvement in the agreement of the model with the experimental response is clearly evident following the identification activity.

Once an identified model with good performance was established, a model order reduction was undertaken. The full finite element model was of 200$^{\text{th}}$ order, which leads to slow simulation and is too large for the model to be included in a real-time control loop. A modal reduction was undertaken on the model of Equation (2), which has eigenvalues and eigenvectors (arranged in order of increasing frequency) denoted as $\mathbf{\Lambda}$ and $\mathbf{V}$ respectively. Defining the modal transformation $\mathbf{z} = \mathbf{V}\mathbf{p}$, a new state space model is derived:

$$\begin{aligned} \dot{\mathbf{p}} &= \mathbf{\Lambda}\mathbf{p} + \mathbf{V}^{-1}\mathbf{B}\mathbf{u} \\ \mathbf{y} &= \mathbf{C}\mathbf{V}\mathbf{p} \end{aligned} \tag{3}$$

Rewriting (3) explicitly separating each term into low and high frequency subset (denoted with $_l$ and $_h$ respectively):

TABLE II
TEST RIG COMPONENT NATURAL FREQUENCIES FROM IDENTIFIED MODEL (FREQUENCIES IN HZ)

	Rotor	Secondary Shaft 1	Secondary Shaft 2
ω_{1x}	46.8	103	114
ω_{1y}	46.8	129	129
ω_{2x}	366	760	774
ω_{2y}	367	805	805

$$\begin{aligned} \begin{bmatrix} \dot{\mathbf{p}}_l \\ \dot{\mathbf{p}}_h \end{bmatrix} &= \begin{bmatrix} \mathbf{\Lambda}_l & \mathbf{0} \\ \mathbf{0} & \mathbf{\Lambda}_h \end{bmatrix} \begin{bmatrix} \mathbf{p}_l \\ \mathbf{p}_h \end{bmatrix} + \begin{bmatrix} \hat{\mathbf{B}}_l \\ \hat{\mathbf{B}}_h \end{bmatrix} \mathbf{u} \\ \begin{bmatrix} \mathbf{y}_l \\ \mathbf{y}_h \end{bmatrix} &= \begin{bmatrix} \hat{\mathbf{C}}_l & \hat{\mathbf{C}}_h \end{bmatrix} \begin{bmatrix} \mathbf{p}_l \\ \mathbf{p}_h \end{bmatrix} \end{aligned} \tag{4}$$

where $\hat{\mathbf{B}} = \mathbf{V}^{-1}\mathbf{B}$ and $\hat{\mathbf{C}} = \mathbf{C}\mathbf{V}$. The cut-off frequency, which demarcates the boundary between the low and high frequency subsets, was chosen as 1 kHz, which is comfortably higher than the largest excitation frequency expected in the system (200 Hz).

The high frequency terms of Equation (4) can now be discarded to yield a far smaller model than the original, in this case with 12 states and thus a 12 $\times$ 12 system matrix. An adjustment must be made to ensure that the truncated model still maintains the same steady state output as the full order model. For this purpose a new matrix, $\mathbf{D}$, is defined, where $\mathbf{D} = -\hat{\mathbf{C}}_h\mathbf{\Lambda}_h^{-1}\hat{\mathbf{B}}_h$, giving the final reduced order model

$$\begin{aligned} \dot{\mathbf{p}}_l &= \mathbf{\Lambda}_l\mathbf{p}_l + \hat{\mathbf{B}}_l\mathbf{u} \\ \mathbf{y}_l &= \hat{\mathbf{C}}_l\mathbf{p}_l + \mathbf{D}\mathbf{u} \end{aligned} \tag{5}$$

Using the final model, the system may be appraised for its natural frequencies; calculated values for each of the three decoupled system component members in each of the x and y axes are presented in Table II. In addition, Figure 6 provides a mode shape plot for the first vibration mode of the system. The plot is made under the conditions that a bias current of 2 A is active in the AMBs such that the rotor and secondary shafts are coupled and form a single system, but no control is applied. It is seen that this mode is dominated by the bending of the rotor (as expected from the lower natural frequency of the rotor compared to the secondary shafts), with almost all the bending concentrated in the narrow central span of the rotor.

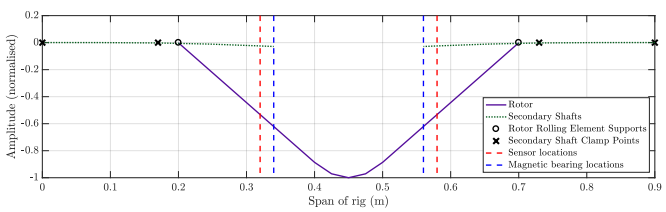

Fig. 6. First vibration mode of experimental system, generated from finite element model enhanced by experimental parameter identification

IV. UNCONTROLLED TEST RIG PERFORMANCE

To establish a baseline behavior of the rotor system presented, three tests were performed, initially without any con-

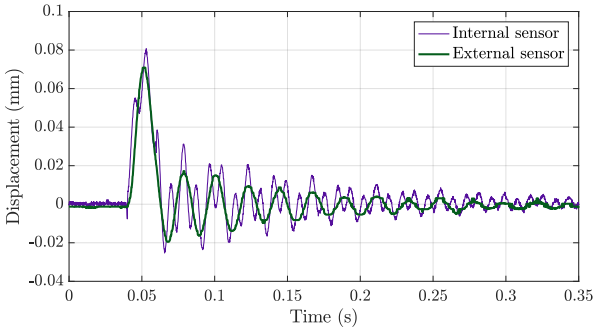

Fig. 7. Time series data showing response in the x_1 axis of the experimental system to an impulse force applied in the x_1 axis, seen from both internally and externally mounted sensors.

trol being applied through the magnetic actuators. Thus in these tests the rotor is supported only by the rolling element bearings at its ends, as indicated in Section II. These bearings are fully located (not loose) in their housings. The experimental tests involved measuring the response of the system to each of the following excitations:

a) An impulse input
b) A variable frequency rotating force on the non-rotating system (forced response test)
c) Synchronous forcing due to rotating unbalance

A. *Impulse Testing*

With the experimental system stationary (no rotation), the magnetic actuators were used to apply an impulse to the system. It was generated by a very short (0.02 s) pulse of current (1 A) supplied to one of the coils in the axis being tested. Each axis was tested separately, with the resulting vibration captured by the transducers aligned in the test axis (one internally mounted, one externally mounted). The captured time series data for this test in the x_1 axis are shown in Figure 7. The response captured by the external sensor is dominated by a single frequency, while the response captured by the internal sensor shows that two frequencies are present. After FFT analysis, the results are presented in Figure 8. Subsequent impulse test results in this paper are presented only as the FFT analysis, without plotting the time series data.

The FFT results clearly demonstrate how the internal and external transducer pairs record different responses. The response in Figure 8a is based on data from the internally mounted transducers, and shows two distinct resonances, one within 40 - 50 Hz, and the other within 110 - 130 Hz. Conversely, Figure 8b is based on data from the externally mounted transducers, and shows only a single resonance within 40 - 50 Hz. This frequency, appearing in both sets of data, is associated with the rotor first natural frequency and correlates with the value indicated by the model of 46.8 Hz. The peak at approximately 120 Hz, however, is associated with the first natural frequency of the secondary shafts, and thus appears only in the results from the internal transducers, which are mounted on this shaft. This result clearly demonstrates that both the rotor and the secondary shafts do indeed exhibit considerable flexible behavior. Good

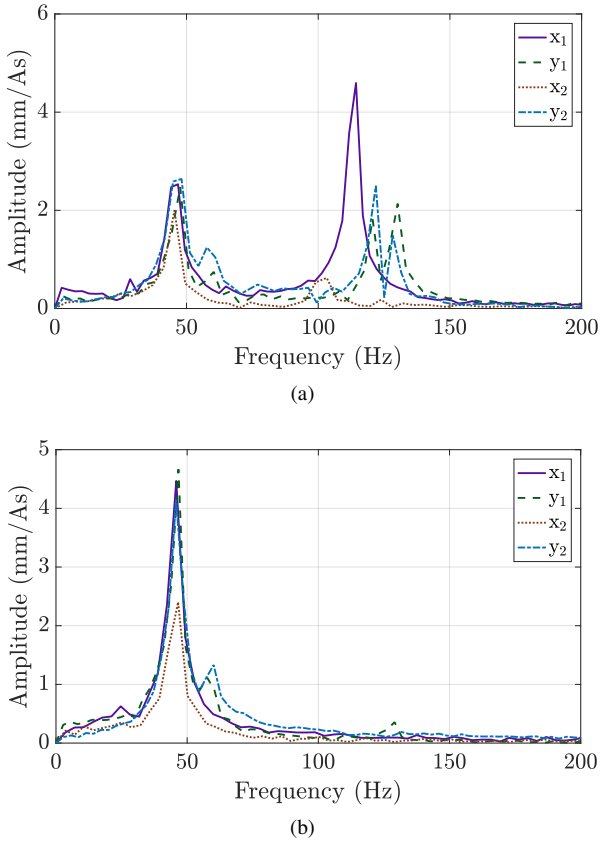

Fig. 8. FFT of impulse response in each test axis without control applied - a) viewed from internally mounted transducers, b) viewed from externally mounted transducers.

correlation is seen between these frequencies and the model-predicted frequencies in Table II.

It is noted further that each of the four actuation/measurement planes (x_1, x_2, y_1, y_2) displays broadly similar behavior, although imperfections in the physical system cause small variations. In Figure 8a it is seen that axis x_1 has a particularly large amplitude at its resonant frequency, while axis x_2 has a notably smaller amplitude response. This is most likely caused by unmodeled nonlinearities in the stiffness properties of the structures which support and clamp the secondary shafts in place.

B. *Forced Vibration Response*

The magnetic bearings were programmed to generate a rotating magnetic field, causing rotating forces acting simultaneously on the rotor and the secondary shafts. The test was run with each of the two magnetic bearings independently.

The testing procedure involved activating the rotating magnetic field over a range of frequencies. At each frequency, once the system had settled to its steady state response, several seconds of transducer data were captured. For this system, excitation frequencies ranging from 1 to 150 Hz were used, covering the first natural frequencies of both the rotor and the secondary shafts.

The results are presented as a set of 2D orbits which vary with the excitation frequency. Each 2D orbit is produced by plotting the x- and y-axis displacement transducer signals

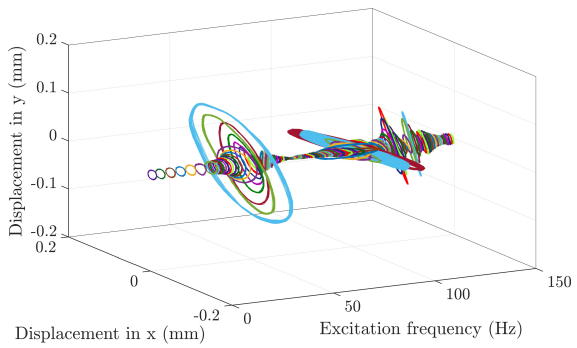

(a)

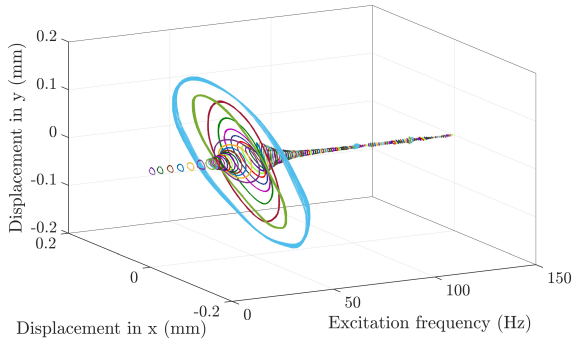

(b)

Fig. 9. Response of uncontrolled static rotor system to forcing imposed through magnetic actuators - a) as seen by internal transducers and b) as seen by external transducers. The colors are for visual enhancement.

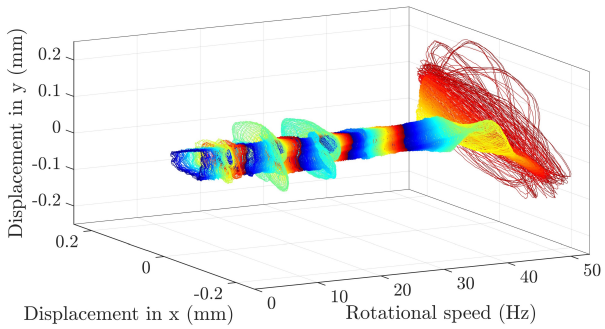

(a)

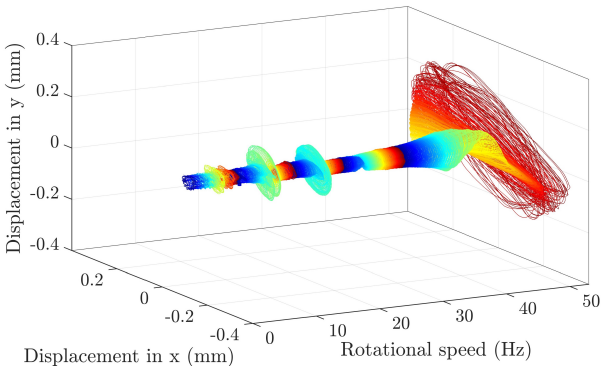

(b)

Fig. 10. Orbits seen during unbalanced rotor run-down with no control active - a) as seen by internal transducers and b) as seen by external transducers. The colors are for visual enhancement.

against each other. These plots can be seen in Figure 9, showing results obtained from End 2 (as defined in Figure 1) from both internal and external reference frames.

C. Rotating Unbalance Response

The rotor was spun up by means of the impulse turbine. The shaft had a residual unbalance calculated to be approximately 50 g.cm, with a total rotor mass of approximately 6 kg.

Data were recorded as the rotor decelerated, i.e. the rotor was spun up to the maximum speed used in the test via manual control of the gas flow over the drive turbine, and then the gas was shut off. Recording the tests like this removes any potential dynamic excitation from the action of the driving gas flow over the turbine.

While the magnetic actuators were inactive, the top attainable rotor speed was approximately 50 Hz, at which point resonant vibration in the rotor caused touchdown contact. This demonstrates that the rolling element bearings do not provide sufficient vibration suppression to allow the rotor to pass its first critical speed. The results of this test are shown in Figure 10. Data presented were taken from End 2 of the rotor, and are presented from both internal and external transducer reference frames. Note that, despite the mechanical bearings, the rotor is still able to undergo significant vibration amplitudes due to its flexible behavior.

The main feature of this result is the large increase in amplitude of the orbits at approximately 50 Hz. It can be noted further that there are two smaller yet clear peaks in response amplitude occurring at lower rotational speeds, namely around 16 and 24 Hz. These frequencies correspond to a third and a half of the rotor natural frequency respectively. Such occurrences are not uncommon in rotor dynamics [36, 37], and are generally found to be associated with nonlinear characteristics in the structure, for instance in the rolling element bearing mounts. A static rotor run-out is also observed, which appears as a low frequency / speed apparent orbit.

V. PD Controlled Experimental System Performance

Classical control algorithms (e.g. PID feedback control) generally work well in AMB systems when the magnetic bearings and displacement transducers are rigidly fixed to a base plate. The standard form of the controller is to set the current in opposing pole pairs to $I_{tot} = I_b \pm I_c$, where I_b is a bias current (2 A in the present system), and I_c is the control current demanded by the controller. In the present case with the flexibly mounted AMB and sensors, no classical controller could be found to generate a suitable control current to permit the rotor to pass its first critical speed. Significant effort was expended to tune experimentally a PD (proportional/derivative) controller (integral control is unnecessary since the rotor is not levitated). A limited range of PD gain values is available, due to the limit of maximum permissible current in the AMB windings. Within this range, high gain values led to instability due to:

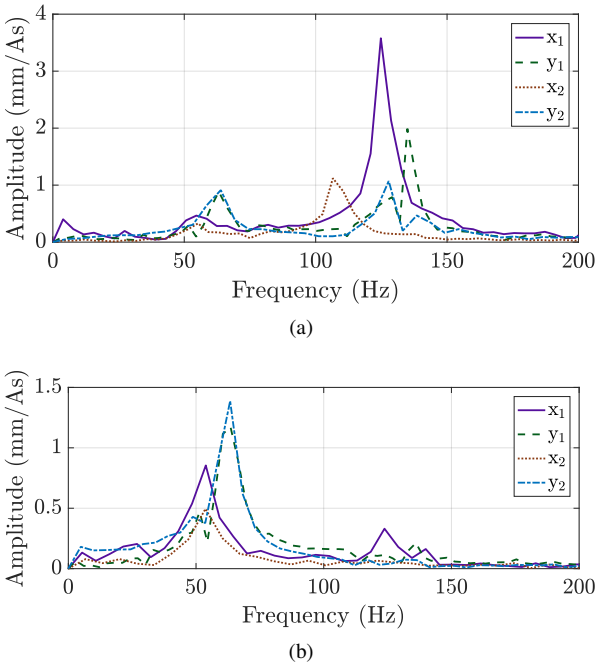

Fig. 11. FFT of impulse response in each test axis with PD control applied - a) viewed from internally mounted transducers, b) viewed from externally mounted transducers.

a) Spillover instability casued by non-colocation of sensor and actuator planes.
b) Imperfect concentricity of the AMB stators within the clearance gap.

After extensive experimentation, the PD gains were chosen as 10 A/mm (proportional) and 0.012 As/mm (derivative) to avoid violating these limits. The derivative filter coefficient was set at 1650 rad/s. The tests undertaken on the uncontrolled rotor were repeated, this time with the chosen PD controller active in the actuators, and the results of these tests are shown in Figures 11 to 13.

In the results of the impulse testing, it is observed that the magnitude of the peak representing the rotor natural frequency is substantially reduced, indicating a significant increase in system damping. There is a small frequency increase of between 10 and 15 Hz associated with this peak.

The forced response results in Figure 12 show that the amplitudes of the response orbits in the region of the rotor first natural frequency are reduced by the control action. However, the responses when the excitation frequency approaches the secondary shaft natural frequency are larger when compared with the results from the uncontrolled system. There is evidence of force being transmitted from the secondary shaft to the rotor (Figure 12b), which is an undesirable effect.

On examination of the results of the response to rotating unbalance, it is clear that the PD controller is capable of only limited reduction of rotor dynamic displacement compared with the uncontrolled case. In accordance with the noted increase of the rotor natural frequency seen in Figure 11, there is a similar increase in the rotational speed at which a resonant response is excited. However, the control action is not able to provide sufficient damping to allow the first critical speed to

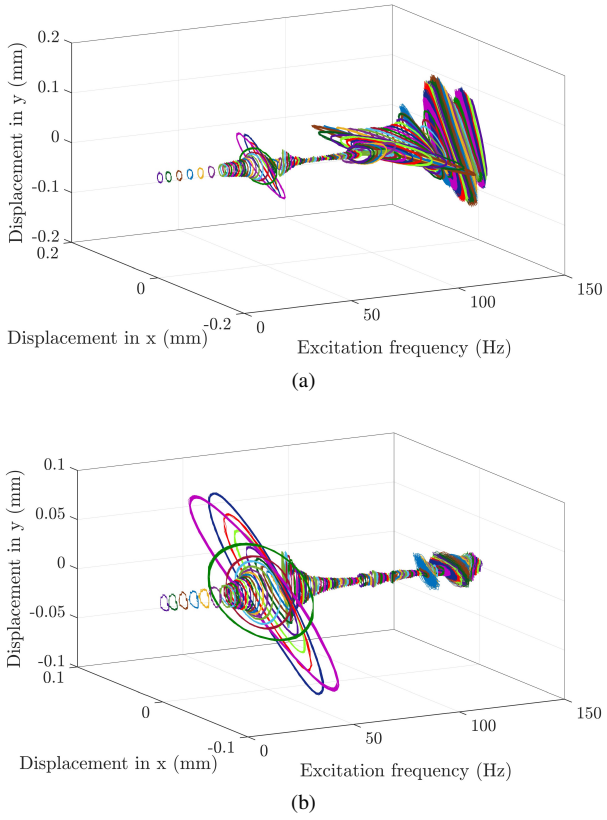

Fig. 12. Response of static rotor system to forcing imposed through magnetic actuators with PD control active - a) as seen by internal transducers and b) as seen by external transducers. The colors are for visual enhancement.

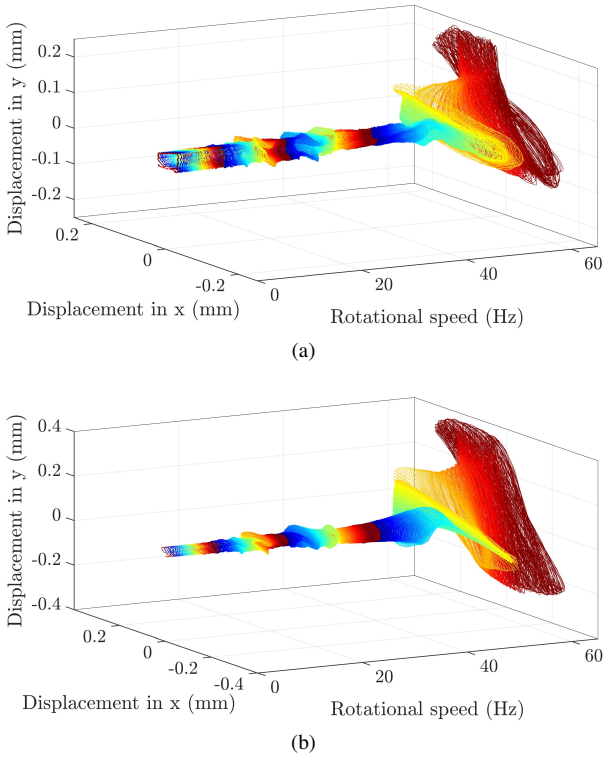

Fig. 13. Orbits seen during unbalanced rotor run-down with PD control active - a) as seen by internal transducers and b) as seen by external transducers. The colors are for visual enhancement.

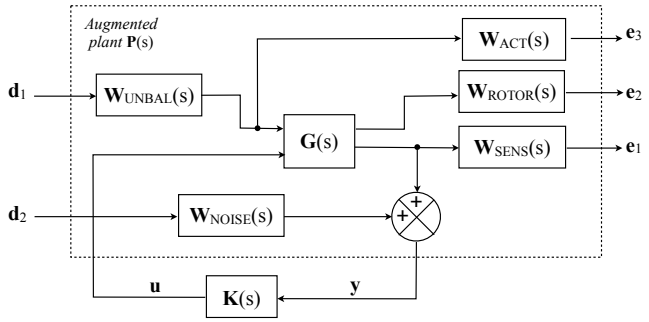

Fig. 14. Structure of plant used to generate H_∞ controller showing location of various weighting functions

be passed altogether, and again rotor/stator contact is evident.

It is observed that all further attempts to achieve significant performance enhancement to the present system with classical control techniques will face a fundamental drawback. Since the feedback signal is a measure of the gap between the rotor and the AMB, both of which exhibit flexible behavior, a classical controller attempting to keep this value constant cannot guarantee minimization of the absolute vibration of the rotor, which is the ultimate goal.

VI. Advancing the Control

To overcome the previously stated limitations, model-based control offers the advantage of built-in observer properties. For this situation, H_∞ optimization allows the expression of performance objectives on the system behavior, which is not possible with simpler classical controllers.

A weighted augmented plant is tailored for the system, as shown in the block diagram in Figure 14. In the diagram, $\mathbf{G}(s)$ is the reduced order plant model as derived in Equation (5) and signals in $\mathbf{d}_1$ and $\mathbf{d}_2$ are disturbances in the form of rotating unbalanced mass and sensor noise respectively. The error signals represent: the displacement of the rotor relative to the magnetic bearing ($\mathbf{e}_1$), the absolute motion of the rotor relative to the ground ($\mathbf{e}_2$) and the demand for control forces with excessively high frequency and/or magnitude ($\mathbf{e}_3$). $\mathbf{y}$ is the output vector fed back to the controller, and $\mathbf{u}$ is the control input force vector.

Once this augmented plant $\mathbf{P}(s)$ is assembled, the H_∞ optimization algorithm attempts to find a controller $\mathbf{K}(s)$ such that the errors $\mathbf{e}_1$, $\mathbf{e}_2$ and $\mathbf{e}_3$ are minimized when the system is subject to the disturbances $\mathbf{d}_1$ and $\mathbf{d}_2$. A crucial characteristic of this augmented plant is that the controller generated ($\mathbf{K}(s)$) only requires signals of relative displacement from the secondary shaft-mounted sensors as its input, but it is still possible to apply a weighting function ($\mathbf{W}_{\text{ROTOR}}$), and thus a performance goal, to the absolution motion of the rotor.

In practical terms, the actual H_∞ optimisation is performed by the built-in Matlab function `hinfsyn`, which takes the augmented plant $\mathbf{P}(s)$ as an input, and delivers the controller $\mathbf{K}(s)$ in state space form as an output. This output can be directly used in the real-time feedback loop to generate a control current I_c, which is combined with a 2 A bias current exactly as with the PD controller.

A. Weighting Function Descriptions

$\mathbf{W}_{\text{ROTOR}}$ is the key weighting of the system It is used to express the target behavior of the rotor. The Bode magnitude plot representing the open-loop response of the rotor model to an unbalance excitation is shown in Figure 15. Based on this response, a transfer function ($\mathbf{T}_{\text{ROTOR}}$) was tuned to express the desired closed loop response. This matches the open-loop performance at most frequencies, but omits the resonant peak. The transfer function determined to describe this goal is

$$\mathbf{T}_{\text{ROTOR}} = 1.73 \times 10^{-7} \frac{(s+900)}{(s+60)} \quad \mathcal{I}_{4\times4} \tag{6}$$

and the Bode magnitude plot of this is included in Figure 15. The performance weighting $\mathbf{W}_{\text{ROTOR}}$ is then set as the reciprocal of this target.

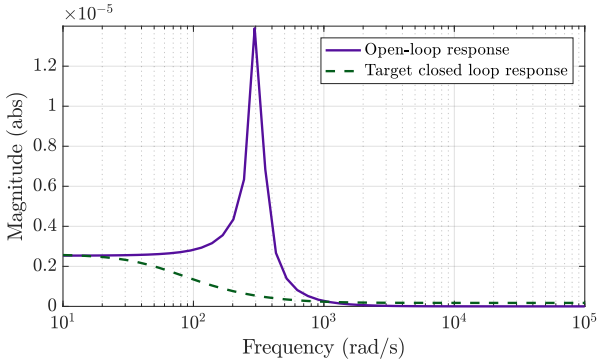

Fig. 15. Bode magnitude plot of rotor open-loop and target closed loop response to unbalance excitation

$\mathbf{W}_{\text{SENS}}$ penalizes relative displacement between the rotor and the secondary shaft which could result in contact. This must be applied uniformly over all frequencies. Touchdown occurs when the relative sensor readings are approximately 0.2 mm. To include a safety margin, 0.15 mm was chosen as the maximum permitted level, hence the weighting is set at the reciprocal of this limit, a constant value of

$$\mathbf{W}_{\text{SENS}} = 667 \quad \mathcal{I}_{4\times4} \tag{7}$$

$\mathbf{W}_{\text{ACT}}$ is used to limit the control forces that the controller may demand, specifically to avoid saturation and overloads. Accordingly, the weighting has a high-pass shape, penalizing heavily signals in and above the kHz zone. It was set as

$$\mathbf{W}_{\text{ACT}} = 100 \frac{(s+7)}{(s+7000)} \quad \mathcal{I}_{4\times4} \tag{8}$$

The expected unbalance force the rotor may experience is described by the weighting $\mathbf{W}_{\text{UBAL}}$. A maximum unbalance 100 g.cm was chosen as a realistic upper limit, and as the force produced is proportional to rotational speed squared, a second order transfer function was used:

$$\mathbf{W}_{\text{UNBAL}} = 1 \times 10^{-3} \frac{s^2}{(\frac{s}{100}+1)^2} \quad \mathcal{I}_{4\times4} \tag{9}$$

The final weighting, $\mathbf{W}_{\text{NOISE}}$, is used to describe the potential transducer noise which may effect the signals provided to the controller. By means of the transfer function

$$\mathbf{W}_{\text{NOISE}} = \frac{1}{s + 1 \times 10^5} + 1 \times 10^{-5} \quad \mathcal{I}_{4\times4} \qquad (10)$$

an expected disturbance on signals of 10 μm amplitude is indicated, coupled with the potential for for a further 10 μm of DC offset due to the rotor-runout.

B. H_∞ Controlled Experimental System Performance

The performance of the H_∞ controller generated was assessed via similar tests to those used for the uncontrolled and PD controlled systems. Results are presented in Figures 16 to 18. The impulse response tests show a significant reduction in amplitude of the rotor natural frequency peak compared to the uncontrolled case. In the response to forced vibration, it is seen that the largest orbits at the rotor resonance are reduced significantly, and also more uniformly circular, than the elliptical responses seen in both the previous test sequences. The more uniform orbits are attributed to the identified model embedded in the controller, adapting the control action to the directional stiffness variations present in the experimental system. It is apparent that the transmission of forces from the secondary shafts into the rotor when the excitation matches the secondary shaft natural frequency is minimal, in contrast to the case with the PD controller.

The rotating unbalance rundown under H_∞ control (Figure 18) demonstrates that the rotor's first critical speed can be surpassed without excessive vibration in either the rotor or the secondary shaft, and also the rotational speed can pass the natural frequency of the secondary shaft without undue vibration occurring. Ultimately, a top rotational speed of 150 Hz (9000 rpm) was reached with the H_∞ controller active, three times the rotor's first critical speed. As this is approaching the upper limit of the rated speed for the rolling element bearings, no further increase was attempted.

The H_∞ controller generated had a tendency to amplify the rotor run-out. However, the amplification observed is not problematic, and the benefits provided by the capability to safely pass the resonance speed outweigh this drawback. There are options to mitigate against this behavior, including activating the controller only when required (i.e. when passing the critical speed), and recording the run-out orbit and subtracting it in real time from the sensor signals.

VII. Conclusions

This paper has presented a system whereby flexibly-mounted internal-stator active magnetic actuators are used for vibration reduction of a flexible rotor. Physical properties of an experimental system demonstrating such a topology have been presented, consisting of a variable diameter steel rotor on rolling element bearings and a pair of magnetic actuators fabricated from SMC and mounted on cantilevered steel shafts.

Techniques used for modeling this system have been outlined, including parameter identification and model order reduction required for model-based control.

The performance of the experimental system with the AMBs inactive was assessed through a series of tests, and it was demonstrated that touchdown contact occurred as the rotor

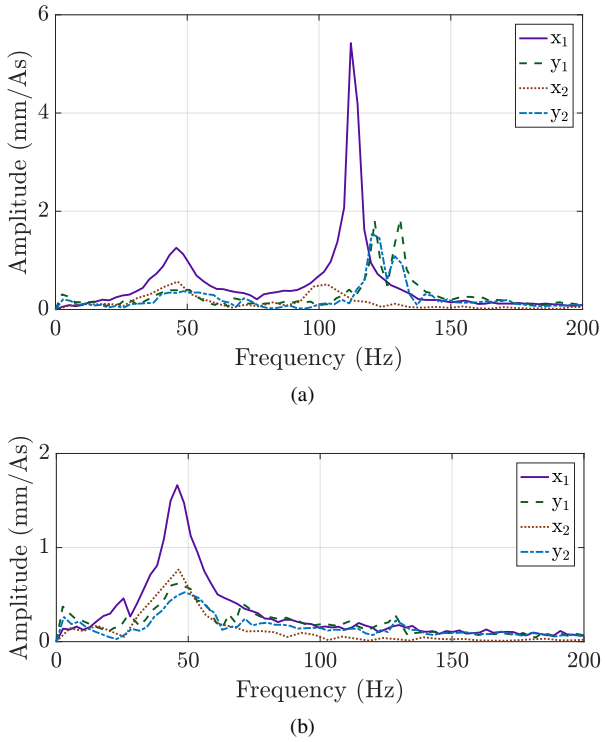

Fig. 16. FFT of impulse response in each test axis with H_∞ control applied - a) viewed from internally mounted transducers, b) viewed from externally mounted transducers.

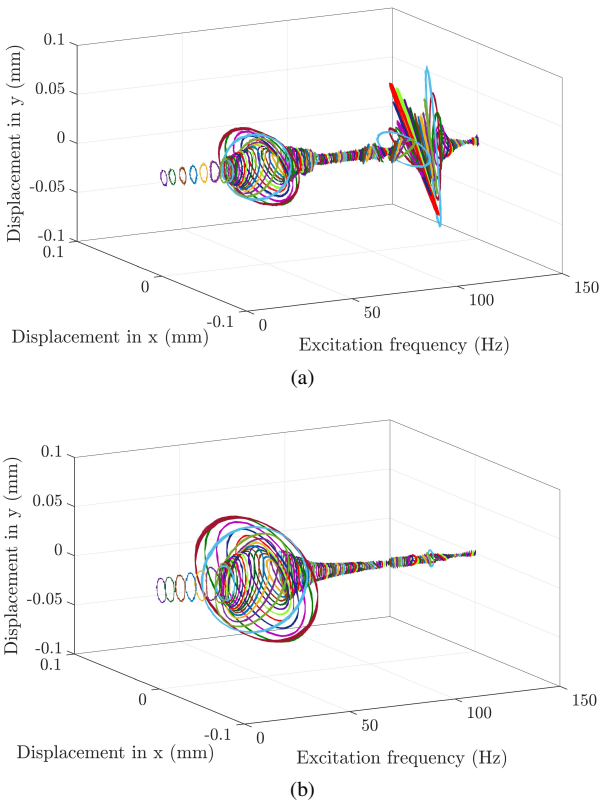

Fig. 17. Response of static rotor system to forcing imposed through magnetic bearings with H_∞ control active - a) as seen by internal transducers and b) as seen by external transducers. The colors are for visual enhancement.

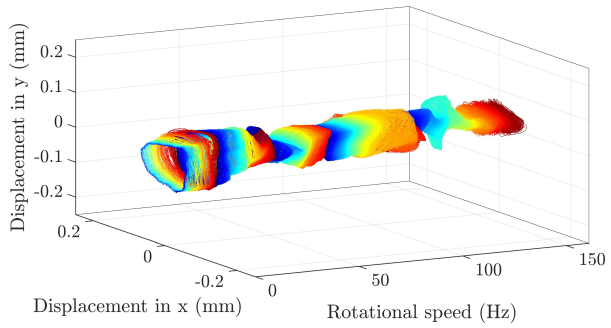

(a)

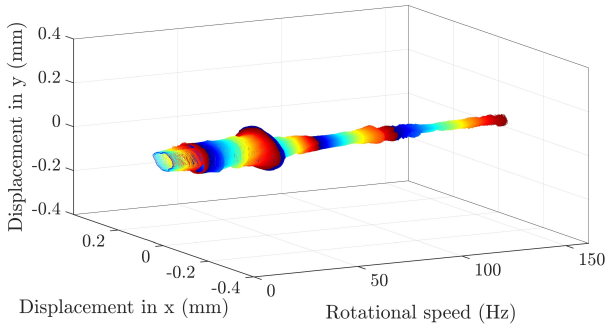

(b)

Fig. 18. Orbits seen during unbalanced rotor run-down with H_∞ control active - a) as seen by internal transducers and b) as seen by external transducers. The colors are for visual enhancement.

approached its first critical speed.

Reducing the rotor's vibration via a PD controller was examined, but while test results show some improved characteristics can be achieved, it was not possible to allow the rotor to pass its first critical speed without touchdown occurring. The resilient mounting of both the magnetic actuators and the displacement transducers contribute to the difficulty experienced by the PD controller.

To address these difficulties, an H_∞ controller based on the identified plant model was generated, with specific details provided regarding the formation of the augmented plant and signal weighting functions. The effectiveness of the H_∞ controller was illustrated definitively through experimental results of the system operating under its influence, whereupon the rotor reached three times its first critical speed in a well controlled manner without any touchdown occurring.

Since the H_∞ controller has a model of the plant embedded in its structure, it was capable of applying control forces to avoid causing problems associated with vibrations of the secondary shafts. The experimental results clearly demonstrate that even when excitations in the neighborhood of the secondary shaft resonant frequency are applied to the system, the H_∞ controller provides superior performance by minimizing the transmission of the secondary shaft vibrations to the rotor.

REFERENCES

[1] W. Rankine, "On the centrifugal force of rotating shafts," *Engineer*, vol. 27, p. 249, 1869.

[2] A. Föppl, "Das problem der lavalschen turbinenwelle," *Der Civilingenieur*, vol. 4, p. 335, 1895.

[3] S. Dunkerley, "On the whirling and vibration of shafts," *Philosophical Transactions of the Royal Society of London. A*, vol. 185, pp. 279–360, 1894.

[4] H. Jeffcott, "The lateral vibration of loaded shafts in the neighbourhood of a whirling speed - the effect of want of balance," *The London, Edinburgh, and Dublin Philosophical Magazine and Journal of Science*, vol. 37, no. 219, pp. 304–314, 1919.

[5] H. Habermann and G. L. Liard, "Control: Practical magnetic bearings: Electronically controlled electromagnets support spinning 1100-kg shafts to micrometer accuracy," *Spectrum, IEEE*, vol. 16, no. 9, pp. 26–30, 1979.

[6] G. Schweitzer, "Magnetic bearings for vibration control," *NASA. Lewis Research Center Instability in Rotating Machinery p 317-326(SEE N 86-30160 21-37)*, 1985.

[7] C. Burrows, M. Sahinkaya, and S. Clements, "Active vibration control of flexible rotors: an experimental and theoretical study," *Proceedings of the Royal Society of London. A. Mathematical and Physical Sciences*, vol. 422, no. 1862, pp. 123–146, 1989.

[8] J. Nikolajsen, R. Holmes, and V. Gondhalekar, "Investigation of an electromagnetic damper for vibration control of a transmission shaft," *Proceedings of the Institution of Mechanical Engineers*, vol. 193, no. 1, pp. 331–336, 1979.

[9] M. Kasarda, P. Allaire, R. Humphris, and L. Barrett, "A magnetic damper for first-mode vibration reduction in multimass flexible rotors," *ASME Journal of Engineering for Gas Turbines and Power*, vol. 112, no. 4, pp. 463–469, 1990.

[10] M. Komori, S. Matsuoka, and S. Fukata, "Evaluations of a hybrid-type superconducting magnetic bearing system," *Applied Superconductivity, IEEE Transactions on*, vol. 6, no. 4, pp. 178–182, 1996.

[11] H. Heshmat, H. M. Chen, and J. F. Walton, "On the performance of hybrid foil-magnetic bearings," in *ASME 1998 International Gas Turbine and Aeroengine Congress and Exhibition*. American Society of Mechanical Engineers, 1998, pp. V005T14A027–V005T14A027.

[12] M. L. Adams, *Rotating Machinery Vibration: From Analysis to Troubleshooting (Mechanical Engineering Series)*, 1st ed. CRC Press, 10 2000.

[13] J. M. Vance, D. Ying, and J. L. Nikolajsen, "Actively controlled bearing dampers for aircraft engine applications," *Journal of Engineering for Gas Turbines and Power*, vol. 122, no. 3, pp. 466–472, 2000.

[14] A. H. Pesch, A. Smirnov, O. Pyrhönen, and J. T. Sawicki, "Magnetic bearing spindle tool tracking through mu-synthesis robust control," *IEEE/ASME Transactions on Mechatronics*, vol. 20, no. 3, pp. 1448–1457, 2015.

[15] E. Maslen, P. Allaire, M. Noh, and C. Sortore, "Magnetic bearing design for reduced power consumption," *Journal of Tribology*, vol. 118, no. 4, pp. 839–846, 1996.

[16] M. N. Sahinkaya and A. E. Hartavi, "Variable bias current in magnetic bearings for energy optimization," *Magnetics, IEEE Transactions on*, vol. 43, no. 3, pp. 1052 –1060, march 2007.

[17] D. Vischer and H. Bleuler, "Self-sensing active magnetic

levitation," *Magnetics, IEEE Transactions on*, vol. 29, no. 2, pp. 1276–1281, 1993.

[18] M. Noh and E. Maslen, "Self-sensing magnetic bearings using parameter estimation," *Instrumentation and Measurement, IEEE Transactions on*, vol. 46, no. 1, pp. 45–50, 1997.

[19] P. García, J. M. Guerrero, F. Briz, and D. D. Reigosa, "Sensorless control of three-pole active magnetic bearings using saliency-tracking-based methods," *Industry Applications, IEEE Transactions on*, vol. 46, no. 4, pp. 1476–1484, 2010.

[20] C. Burrows, P. Keogh, and M. N. Sahinkaya, "Progress towards smart rotating machinery through the use of active bearings," *Proceedings of the Institution of Mechanical Engineers, Part C: Journal of Mechanical Engineering Science*, vol. 223, no. 12, pp. 2849–2859, 2009.

[21] E. Maslen, G. Schweitzer, H. Bleuler, M. Cole, P. Keogh, R. Larsonneur, R. Nordmann, Y. Okada, and A. Traxler, *Magnetic bearings: theory, design, and application to rotating machinery*. Springer-Verlag Berlin Heidelberg, 2009.

[22] R. Stanway and C. Burrows, "Active vibration control of a flexible rotor on flexibly-mounted journal bearings," *Journal of Dynamic Systems, Measurement, and Control*, vol. 103, no. 4, pp. 383–388, 1981.

[23] S. Sivrioglu and K. Nonami, "Sliding mode control with time-varying hyperplane for amb systems," *IEEE/ASME Transactions On Mechatronics*, vol. 3, no. 1, pp. 51–59, 1998.

[24] Y. Le and K. Wang, "Design and optimization method of magnetic bearing for high-speed motor considering eddy current effects," *IEEE/ASME Transactions on Mechatronics*, vol. 21, no. 4, pp. 2061–2072, 2016.

[25] L. Quurck, H. Schaede, M. Richter, and S. Rinderknecht, "High speed backup bearings for outer-rotor-type flywheels – proposed test rig design," in *Proceedings of 14th International Symposium on Magnetic Bearings*, 2014, pp. 109–114.

[26] T. Yamada, Y. Nakano, J. Asama, A. Chiba, T. Fukao, T. Hoshino, and A. Nakajima, "Outer rotor consequent-pole bearingless motor with improved start-up characteristics," *IEEE Transactions on Magnetics*, vol. 44, no. 11, pp. 4273–4276, 2008.

[27] J.-H. Lee, C.-B. Park, B.-S. Lee, S.-G. Lee, J.-H. Kim, S.-M. Jung, and H.-W. Lee, "A study on the design procedure of the eight pole magnetic bearings for the inner-rotor and the outer-rotor type," *Journal of Electrical Engineering and Technology*, vol. 8, no. 6, pp. 1424–1430, 2013.

[28] C. Liu and G. Liu, "Field dynamic balancing for rigid rotor-amb system in a magnetically suspended flywheel," *IEEE/ASME Transactions on Mechatronics*, vol. 21, no. 2, pp. 1140–1150, 2016.

[29] P. Peralta, T. Wellerdieck, D. Steinert, T. Nussbaumer, and J. W. Kolar, "Ultra-high temperature (250c) bearingless permanent magnet pump for aggressive fluids," *IEEE-ASME Transactions on Mechatronics*, vol. 22, no. 5, pp. 2392–2394, 2017.

[30] L. Quurck, M. Richter, M. Schneider, D. Franz, and S. Rinderknecht, "Design and practical realization of an innovative flywheel concept for industrial applications," *Power*, vol. 50, p. 100, 2017.

[31] C. Lusty, M. Sahinkaya, and P. Keogh, "A novel twin-shaft rotor layout with active magnetic couplings for vibration control," *Proceedings of the Institution of Mechanical Engineers, Part I: Journal of Systems and Control Engineering*, vol. 230, no. 3, pp. 266–276, 2016.

[32] C. Lusty and P. Keogh, "Vibration reduction in a hollow-shaft rotor using flexibly-mounted internal-stator magnetic bearings," *JSME Mechanical Engineering Journal*, vol. 4, no. 5, pp. (advanced publication DOI: 10.1299/mej.17–00 008), 2017.

[33] V. Gondhalekar and R. Holmes, "Design of a radial electromagnetic bearing for the vibration control of a supercritical shaft," *Proceedings of the Institution of Mechanical Engineers, Part C: Journal of Mechanical Engineering Science*, vol. 198, no. 4, pp. 235–242, 1984.

[34] H. Nelson and J. McVaugh, "The dynamics of rotor-bearing systems using finite elements," *ASME Journal of Engineering for Industry*, vol. 98, pp. 593–600, 1976.

[35] J. Lauridsen, A. Sekunda, I. Santos, and H. Niemann, "Identifying parameters in active magnetic bearing system using lft formulation and youla factorization," in *2015 IEEE Conference on Control Applications (CCA)*. IEEE, 2015, pp. 430–435.

[36] D. Bently, "Forced sub-rotative speed dynamic action of rotating machinery," in *MECHANICAL ENGINEERING*, vol. 96, no. 10. ASME-AMER Soc Mechanical Eng 345 E 47th St, New York, NY 10017, 1974, pp. 60–60.

[37] D. W. Childs, "Fractional-frequency rotor motion due to nonsymmetric clearance effects," *Journal of Engineering for Power*, vol. 104, no. 3, pp. 533–541, 1982.

PLACE PHOTO HERE

Chris Lusty received MEng and PhD degrees in Mechanical Engineering from the University of Bath, U.K. in 2012 and 2016 respectively.

He is currently a Research Associate at the University of Bath, U.K., and pursues interests in magnetic bearings, rotor dynamics, vibration control and mechatronic system design.

PLACE PHOTO HERE

Patrick Keogh received a B.Sc. degree in mathematical physics from the University of Nottingham, Nottingham, U.K., in 1979, and a Ph.D. degree in applied mathematics from the University of Manchester, Manchester, U.K. in 1983.

He was a Research Technologist at the Alstom Engineering Research Centre, Stafford, Stafford, U.K. In 1990, he joined the Department of Mechanical Engineering, University of Bath, Bath, U.K. His current research interests include rotor dynamics, magnetic bearing systems, active vibration control, optimal control for multivariable systems, contact dynamics, and associated dynamic behavior of rotor touchdown bearings.